NASA TECHNICAL NOTE

NASA TN D-5265

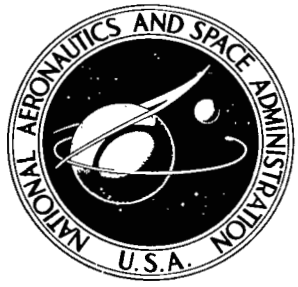

A BRUSHLESS DC TORQUER-DRIVEN REACTION WHEEL FOR SPACECRAFT ATTITUDE CONTROL

by R. Fulcher

Goddard Space Flight Center
Greenbelt, Md.

NATIONAL AERONAUTICS AND SPACE ADMINISTRATION • WASHINGTON, D. C. • JULY 1969

A BRUSHLESS DC TORQUER-DRIVEN REACTION WHEEL FOR SPACECRAFT ATTITUDE CONTROL

By R. Fulcher

Goddard Space Flight Center
Greenbelt, Md.

NATIONAL AERONAUTICS AND SPACE ADMINISTRATION

For sale by the Clearinghouse for Federal Scientific and Technical Information
Springfield, Virginia 22151 – CFSTI price $3.00

ABSTRACT

As a further development of electromechanical direct drive systems for space applications, dc photoelectronic (brushless) commutation techniques have been applied to the design of a reaction wheel. The resulting prototype hardware, which also incorporates optimized mechanical features, is shown to compare favorably on a weight/power basis with currently used ac torquer-driven reaction wheels. Furthermore, full utilization of the brushless commutator has simplified and improved control systems by providing, within the reaction wheel itself, the control electronic functions of bi-directional rotation, torque level control, and power amplification. A test control system using a prototype brushless reaction wheel on a single-axis platform demonstrated excellent dynamic response and high pointing accuracy (within a few seconds of arc). Life testing of prototype hardware has been underway for 2 years.

CONTENTS

A BRUSHLESS DC TORQUER-DRIVEN REACTION WHEEL FOR SPACECRAFT ATTITUDE CONTROL

by
R. Fulcher
Goddard Space Flight Center

INTRODUCTION

A frequently used form of spacecraft attitude control employs reaction wheels. These devices are motor-driven flywheels that are accelerated to apply continuously controllable torques to a spacecraft by means of reaction on the spacecraft structure. Since reaction wheels are powered by electrical power that can be replenished in space by solar energy, their only major operational limitation occurs when the "flywheel" reaches the maximum angular speed of the selected drive motor; no further flywheel acceleration is then possible. To operate within this limitation, a reaction wheel control system typically is used in conjunction with a secondary torque source (e.g., gas jet system) that keeps the flywheel speed always below the limiting speed.

This document presents a basic design for a reaction wheel that utilizes a photoelectronically commutated (brushless) dc torquer for the drive motor. Prototype-quality reaction wheels with varying electrical characteristics have been produced from this design, one of which is shown (partially disassembled) in Figure 1.

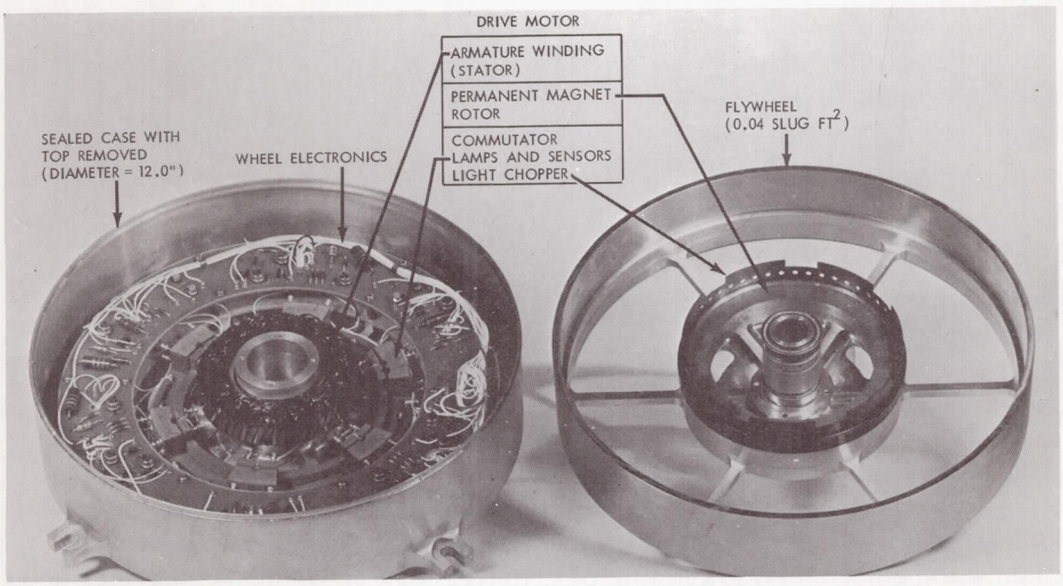

Figure 1 — Prototype brushless dc torquer-driven reaction wheel.

To ensure that spacecraft control system needs are met most effectively, the reaction wheel is designed to satisfy two objectives–(1) provide a torque transducer that produces a linear, symmetrical torque response proportional to a low-level control signal, and (2) provide an electromechanical energy converter that has high efficiency, minimum weight, and high reliability. How well these objectives are met depends greatly upon the drive motor selected. It is believed that the selected motor, a brushless dc torquer, is the optimum choice for a spacecraft reaction wheel. First, being a permanent magnet design, this torquer has an inherent characteristic torque constant that provides the desired proportional output when the armature current is controlled by a signal voltage. By using the torquer as a generator, a symmetrical torque response is provided about any flywheel speed. Second, as a converter of electrical energy to mechanical energy, the permanent-magnet design is the most efficient for a given size, weight, and speed since the field flux is passive and requires no power to maintain. Also this torquer has a regenerative braking mode that can provide an additional power savings when generator action is possible. Photoelectronic commutation integrates this efficient, linear torque-producing device with the available dc power and low-level signal commands. Reliability is improved since the number of functional elements needed to effect the desired attitude control are minimized. As a drive motor, the brushless dc torquer of "pancake" geometry readily permits a direct match of motor and load. This eliminates the need for any intermediate gearing thus removing a source of mechanical inefficiency and backlash.

When the brushless reaction wheel is used in a closed-loop control system, error-rate compensation provides the servo damping. This avoids the deterioration of response near zero speed that is typical of tachometer feedback systems. The system weight also is reduced since the size and weight of an electromagnetic tachometer are considerable when low-speed sensitivity is necessary. For telemetry purposes, the brushless reaction wheel has a photoelectronic tachometer that provides an analog signal representative of flywheel speed. The photoelectronic tachometer also provides a unique digital output as a function of direction; this output is used in the control circuitry to reduce the effect of coulomb friction and to provide regenerative braking.

Operating the prototype reaction wheels in closed-loop pointing tests on ground simulators has demonstrated their effectiveness as attitude-control actuators. They have achieved significant power and weight savings over similar devices currently in use.

DESIGN

A reaction wheel is required to provide sufficient torque and angular momentum to fulfill an operational requirement. The significance of these two quantities in terms of reaction wheel design can be seen by reference to Figure 5. The "peak operational torque" shown is directly related to the desired spacecraft control system response time. The second quantity, angular momentum, is determined by the external disturbance torque acting upon a spacecraft, the control system maneuvering requirements, and the choice of secondary torque source to be used in conjunction with the reaction wheel control system. Reaction wheel angular momentum is defined by the product of the "maximum speed" shown in Figure 5 and the moment of inertia of the flywheel. It should be noted that the maximum speed is the greatest flywheel speed at which the required peak operational torque can still be developed. The reaction wheel design problem can thus be defined as that of supplying the required operational torque and angular momentum with a minimum of weight, power consumption, and control nonlinearities; and with maximum reliability.

Mechanical Design

The essential features of the basic mechanical design of the brushless reaction wheel are illustrated in Figure 1. As seen, the three subassemblies are the drive motor and wheel electronics, the flywheel, and the sealed case. Rather than dwell upon details of the mechanical design, this section emphasizes the procedures that were used to optimize the basic design.

Two key decisions in the mechanical design are to choose a diameter for the reaction wheel case and to choose the maximum flywheel speed previously mentioned. As will be seen, these choices can lead to a reaction wheel design that satisfies operational requirements for torque and angular momentum while minimizing system weight and power requirements.

A starting point for the optimizing procedure is to recognize that for any given flywheel moment of inertia and any given case height, a case diameter can be found which minimizes the weight of the flywheel and case combined. This is illustrated in Figure 2. The case weight curve shown was plotted readily by assuming that the case consisted of a cylindrical shell closed at the ends by circular cover plates. The weight of such a case, W_c, is

$$W_c = \text{shell weight} + \text{end plates' weight}$$

$$= \pi D L t_c w_c + 2\left[\frac{\pi D^2}{4} t_c w_c\right] ,$$

where

D is the mean diameter of the shell,

L is the case height assumed (3 inches),

t_c is the case thickness assumed (0.125 inch),

and

w_c is the weight-density of the case material (assumed to be aluminum = 0.10 lb/cu in.).

The flywheel weight curve shown was plotted by assuming the flywheel to be a homogeneous, *hollow* right circular cylinder of outer and inner radii R and r, respectively. Rearranging the well known formula for the moment of inertia of such a cylinder yields the expression used to plot the flywheel weight W_F:

$$W_F = \frac{2gI_F}{R^2 + r^2} ,$$

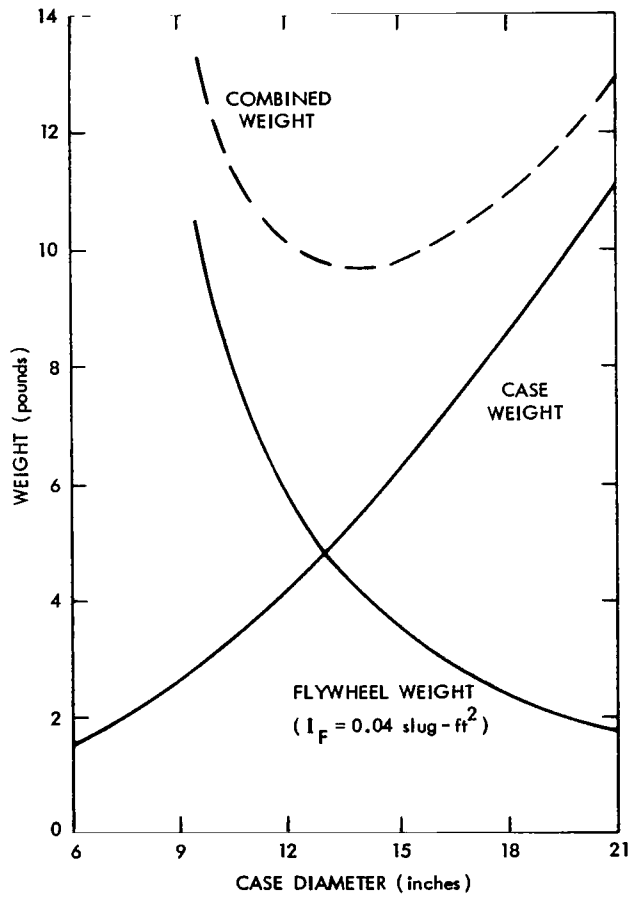

Figure 2 — Weight of flywheel and case versus case diameter.

where

I_F is the flywheel moment of inertia about the axis of interest, and

g is the acceleration of gravity.

In order to use the foregoing expression for flywheel weight, it is necessary to determine r, once R and I_F are specified. This was done by using a second expression for flywheel weight:

W_F = product of flywheel weight-density and volume

$$= w_F \left[\ell\pi(R^2 - r^2)\right] ,$$

where

ℓ is the height of the flywheel assumed (2.50 inches), and

w_F is 0.28 lb/cu. in. (flywheel material assumed to be stainless steel). Combining the two preceding expressions for flywheel weight gives the desired solution for r:

$$r = \sqrt[4]{R^4 - \frac{2gI_F}{w_F \pi \ell}}$$

The flywheel weights plotted in Figure 2 as a function of case diameter, D, are not plotted directly at the 2R values, but rather include an adjustment along the abscissa scale of 0.50 inch, to account for mechanical clearance between the flywheel and case. Also, it should be realized that a family of curves for flywheel weight could have been drawn in Figure 2 for various flywheel moments of inertia; the case weight would still be a single curve.

A comprehensive optimization can now be made on the basis of a selected case diameter. This is illustrated in Figure 3 which applies to the 12-inch case diameter selected for the basic mechanical design. Here the abscissa scale represents the trade-off of supplying the specified reaction wheel angular momentum (assumed to be 1.05 ft-lb-sec) with greater flywheel maximum speed or greater flywheel moment of inertia. This trade-off exists because, as noted earlier, reaction wheel angular momentum is defined by the product of flywheel maximum speed and moment of inertia. Thus, every point on the abscissa scale satisfies the specified angular momentum. The flywheel and case weight plots shown in Figure 3 include the 12-inch diameter values from

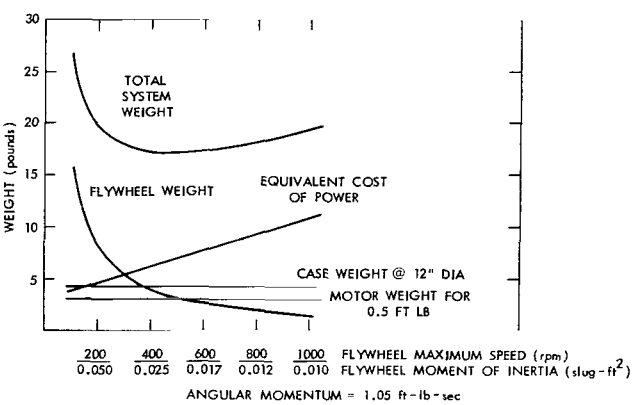

Figure 3 — Reaction wheel optimization for a selected case diameter.

Figure 2, but the flywheel weight curve in Figure 3 is expanded to include several flywheel moments of inertia, all for the 12-inch case diameter. These flywheel weights relate to the family of curves that could have been made in Figure 2. They were computed using the previously given expression for flywheel weight, but with I_F as the variable rather than R. The motor weight plot in Figure 3, a straight line, shows that a drive motor that fits within the 12-inch case diameter and produces the specified operational torque (assumed to be 0.5 ft-lb) can be considered to have a constant weight. The cost of having the motor produce the operational torque at greater and greater maximum speeds is proportionately greater electrical power. To include this motor power in the optimization, the power requirements have been converted into an equivalent weight requirement. For example, spacecraft solar cell power systems are often expressed in pounds of power system required per unit watt of electrical power generated. The equivalence ratio used here is shown by the equivalent cost of power curve in Figure 3. At this point, all of the curves in Figure 3 can be added to develop the total system weight curve shown, which enables the optimum (minimum weight) point to be determined by inspection. This abscissa value then defines the optimum reaction wheel parameters that satisfy the operational torque and angular momentum requirements.

The equation for flywheel weight was also used to determine the desirability of high-density metals for the flywheel material. As is seen in Figure 4, when the flywheel thickness, t_F (equal to R – r), is small compared to the flywheel diameter, little is gained by the use of high-density metals. The material choices for the basic mechanical design of the reaction wheel were aluminum for the sealed case and stainless steel for the flywheel.

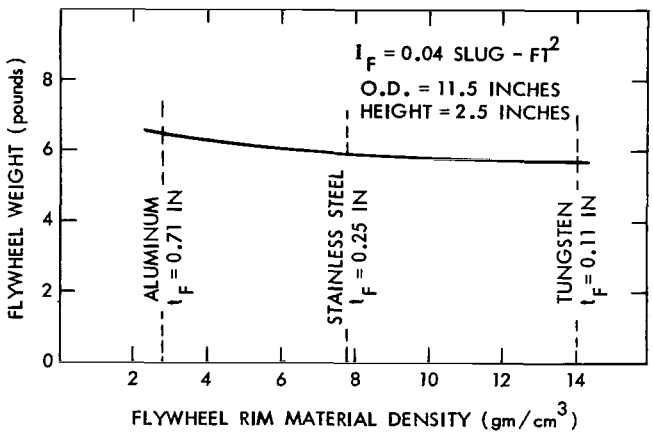

Figure 4— Weight of flywheel versus rim density.

A critical aspect of reaction wheel mechanical design is the flywheel bearings. The maximum flywheel speed determined by the foregoing optimization must be examined to ensure that it is compatible with reliable bearing design. In the basic design of the brushless reaction wheel, maximum speeds of up to 1000 rpm were considered conservative for 1-year missions. The basic design has a sealed case to permit the use of conventionally lubricated ball bearings. They have inner race rotation and are preloaded at 20 pounds to remove radial play. Bearing and windage losses together are 0.0047 ft-lb, which is less than 1 percent of the drive motor peak torque.

The advantageous thermal aspects of the basic mechanical design of the brushless reaction wheel should be noted. Heat transfer cannot be a problem with the rotating portion of the reaction wheel since the brushless dc torquer has no power dissipation in the permanent-magnet rotor. In the nonrotating portion of the reaction wheel where heat must be dissipated from the torquer stator (Figure 1) the stator mount is integral with the housing and provides an excellent, thermally conductive path to the base and mounting lugs. The thermal design also provides a separate support for the flywheel bearings, which removes them from the thermally conductive path from the torquer stator to the mounting lugs.

Drive Considerations

The photoelectronically commutated dc torquer selected for the reaction-wheel drive very nearly provides the idealized function of a bilateral torque transducer, in which torque output is a function of input error signal only. Output torque is relatively unaffected by angular position or velocity of the rotor and other conditions such as power supply voltage. The photoelectronic commutator eliminates the brush friction and wear normally associated with dc torquers. Significant advantages for attitude-control applications result:

1. Attitude control system design can be simplified since loop gain and torque null are not a function of the variables mentioned.

2. For spacecraft missions requiring constant velocity slewing, following error is minimized since the viscous damping is small.

The selected torquer further enhances attitude-control applications in many ways. The photoelectronic commutator has integrated within it bidirectional wheel rotation capability and the functions of torque-level control, power amplification, and regenerative braking. All of this is accomplished with practically no increase in commutator complexity, thereby enhancing overall control system reliability and providing savings in system weight and power. The commutator is compatible with both the low-level control signal input and the dc power normally available directly from spacecraft power supplies.

Figure 5 shows the torque-speed characteristics of a brushless dc torquer used in one of the prototype reaction wheels. Greatly different electrical characteristics were obtained for other prototypes by merely selecting another winding, indicating the flexibility of the basic torquer design. The desired constant-torque characteristic is obtained from the typical torquer characteristic (shown by the broken line in Figure 5) by controlling the base voltage of the photoelectronic commutator power switch driver transistor. This control technique is possible since the dc torquer has a developed torque per ampere of armature current that is independent of the rotor speed. The "operating region" in Figure 5 is defined by the four-quadrant zone bounded by the peak torque and the maximum speed at which this torque can be provided. The I^2R losses in the torquer affect the size of the operating region but not operation within these limits.

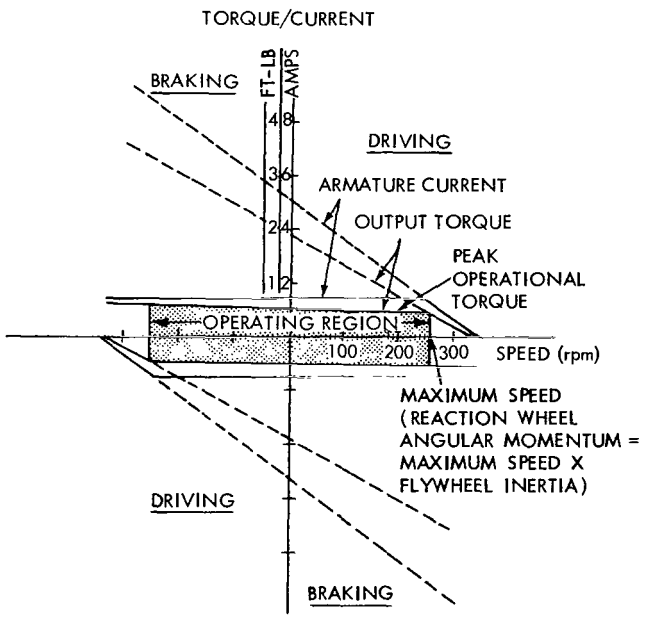

Figure 5 — Reaction wheel brushless dc torquer characteristics.

Figure 5 illustrates the negative speed (braking) regions where mechanical energy stored in the flywheel is potentially available to assist braking. The ability of the brushless dc torquer to operate equally effectively as a generator has been used to enable a regenerative braking mode. The unique feature of this mode is that electrical braking power is supplied by the reaction wheel itself, rather than placing the full demand upon the external power supply. In applications such as spacecraft scanning where velocity changes are frequent, the overall system efficiency can be increased by this capability.

Comparison With Current Designs

The mechanical and electrical design effort has resulted in a reaction wheel that compares favorably with current designs. There follows a comparison of one of the hardware prototype brushless reaction wheels produced from the basic design with reaction wheels used in a number of NASA missions.

The first comparison is one of weight and power requirements versus quantities provided by each of the reaction wheels. These quantities which a reaction wheel must provide are angular momentum and operational torque, as pointed out in the previous discussion on reaction wheel design. The comparison based upon this rationale is presented in Figure 6 and illustrates that reaction wheels which exceed the brushless reaction wheel in torque or angular momentum require significantly more weight and power. A tacit assumption in the foregoing comparion is that spacecraft design constraints in each case allowed an optimized reaction wheel design.

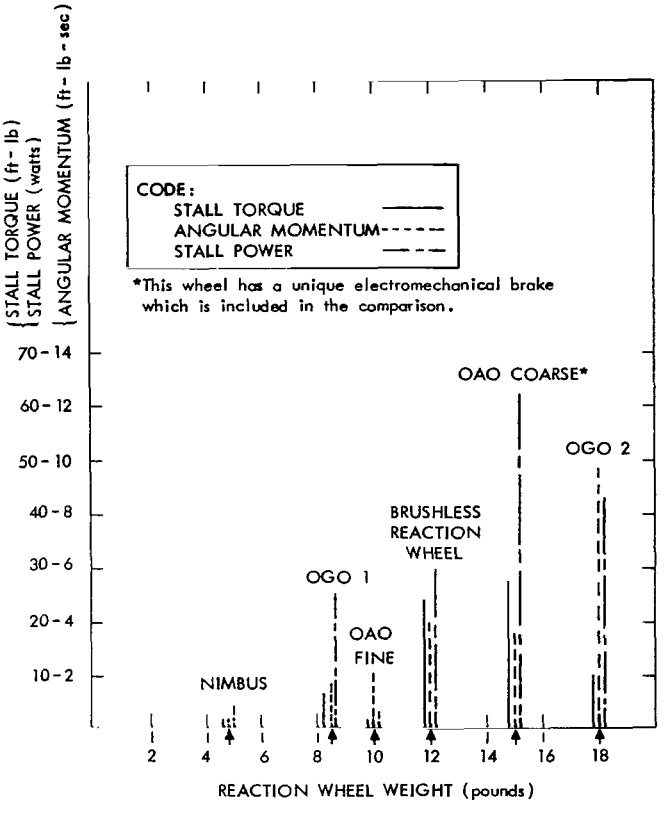

Figure 6— Weight-power comparison with current reaction wheels.

A second comparison with the same reaction wheels is based upon electromechanical efficiency. This is shown in Figure 7. Here the relative efficiency of electromechanical energy conversion is compared by referencing mechanical output at 1000 rpm. The torque per watt at this speed is thereby a direct indication of electromechanical efficiency. The favorable value shown in Figure 7 for the brushless reaction wheel does not include the energy savings possible from the regenerative braking capability built into the brushless reaction wheel. For spacecraft scanning missions, this capability is estimated to yield up to a 30-percent power savings.

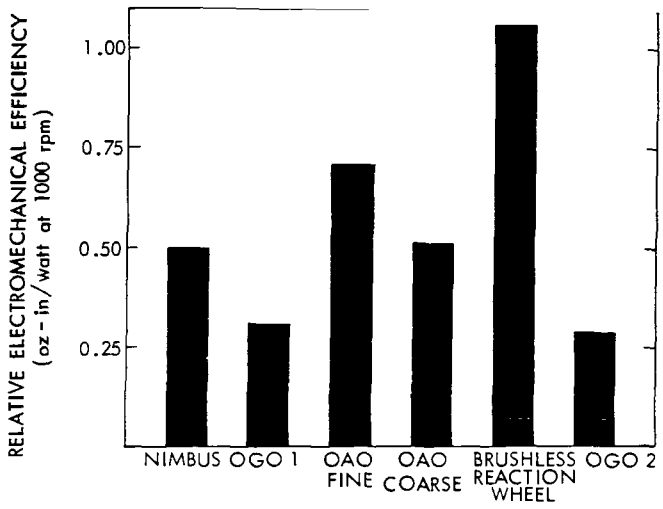

Figure 7— Comparison of relative efficiency with current reaction wheels.

The suitability of the brushless reaction wheel for long-term space missions has been documented in reliability calculations of report NAS CR 388.* Also, life testing of one of the prototype reaction wheels has been proceeding successfully for over 2 years.

PERFORMANCE

The brushless reaction wheel was developed to be the actuator in high-accuracy spacecraft attitude-control systems. The prototype reaction wheels were to be capable of scanning and maintaining the orientation of large spacecraft. To verify the anticipated performance. one of the prototype reaction wheels was tested in a control loop on an essentially torque-free table.

Control System

Figure 8 is a block diagram of the test system. Details concerning the sensor and control electronics blocks are presented in Appendix A. The function of the system was to orient the bifilar suspended, single-axis table (25 slug-ft^2 moment of inertia). The autocollimator sensor was aimed down the axis of suspension. The system reaction torque (at zero speed) as a function of error voltage, V_e, is shown in Figure 9.

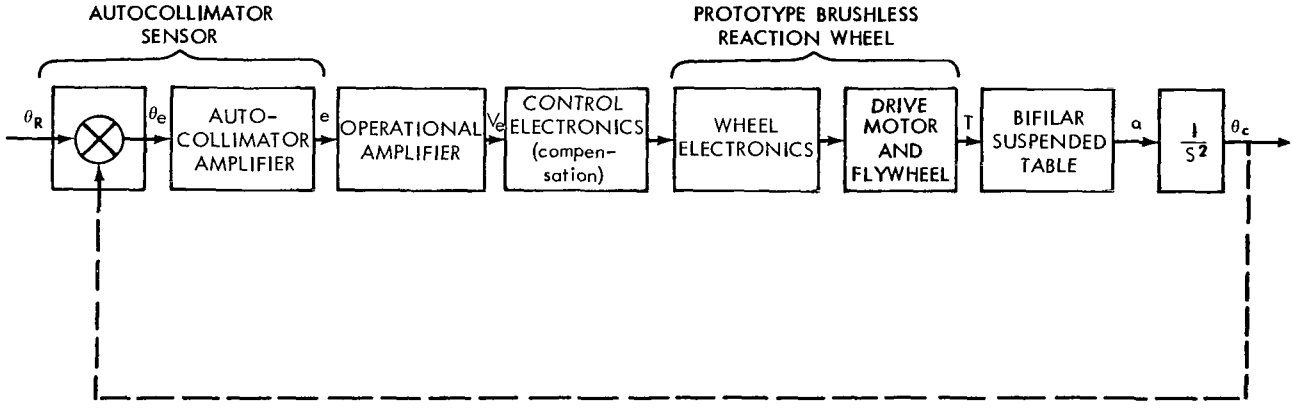

Figure 8— Test control loop.

* W. M. Casady, "Reaction Wheel with Brushless DC Motor Drive," Sperry Farragut Co., NAS 5-9016, April 1966 (Available through Clearinghouse for Federal Science & Technical Information, Springfield, Virginia).

Closed-Loop Tests

The system was subjected to sinusoidal, triangular, and square-wave commands; it produced the responses shown in Figure 10. In the analysis of the test data which follows, the small viscous damping term associated with the brushless reaction wheel was neglected.

The frequency response (Figure 11) was plotted from recorded data obtained when the system was subjected to the sinusoidal command. The natural frequency f_N is

$$f_N = \frac{f\,(\text{amplitude ratio} = 1{:}1)}{\sqrt{2}}$$

$$= \frac{1.06\ \text{Hz}}{\sqrt{2}} = 0.750\ \text{Hz}\ ;$$

$$\omega_N = 4.71\ \text{rad/sec.}$$

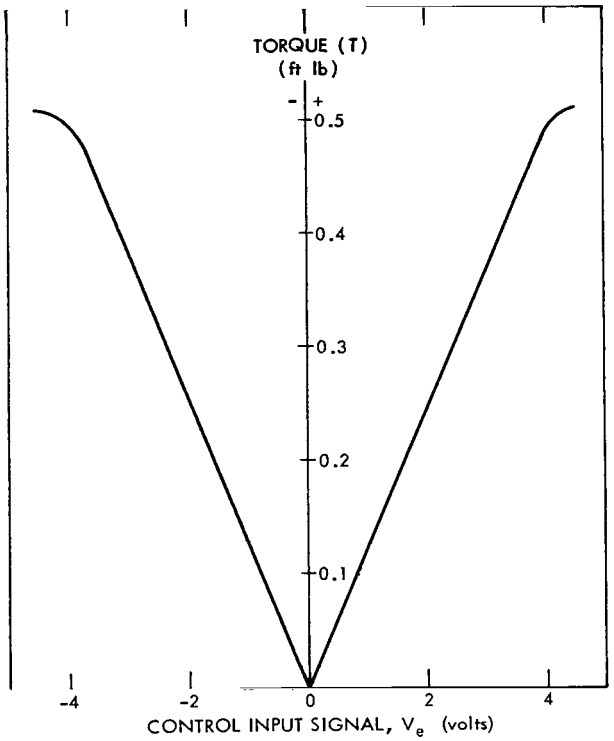

Figure 9— Control loop gain characteristic.

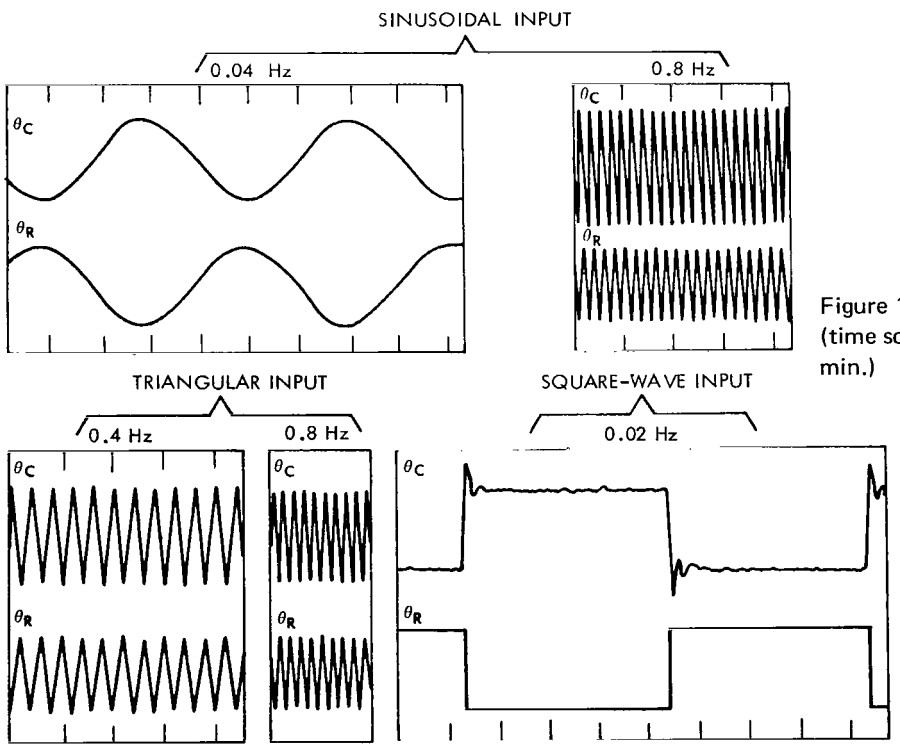

Figure 10—Typical system responses (time scale for all graphs is 100 mm/min.)

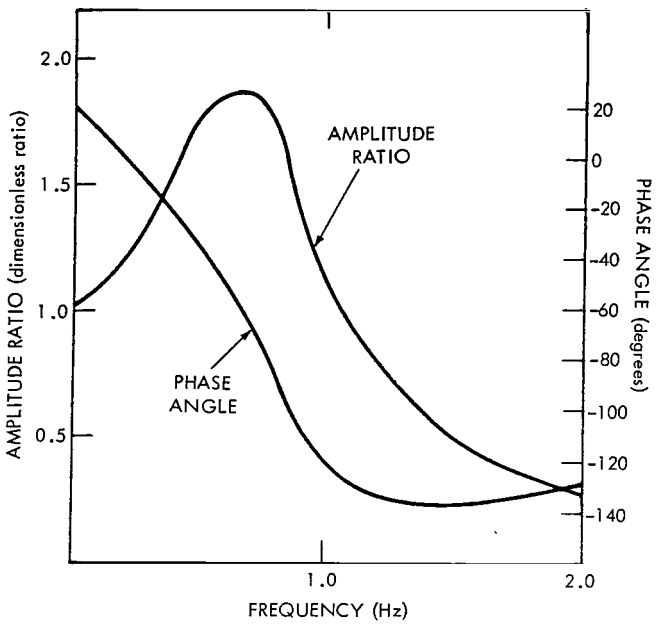

Figure 11 — System frequency response.

Comparison with universal curves of frequency response indicates a damping ratio, c, of 0.35. With this damping, the frequency for maximum amplitude is found to be

$$\frac{f_{A_{max}}}{f_N} = \frac{1}{2c}\sqrt{\sqrt{8c^2 + 1} - 1} = 0.910 \quad ,$$

and

$$f_{A_{max}} = 0.682 \text{ Hz.}$$

The maximum amplitude of response is

$$A_{max} = \sqrt{\frac{8c^4}{\sqrt{8c^4 - 4c^2 - 1 + \sqrt{8c^2 + 1}}}}$$

$$= 1.88 \ .$$

This computed point (f = 0.682 Hz, A = 1.88) was used in plotting the amplitude ratio curve of Figure 11. The phase angle portion of the figure shows the influence of the error rate network. First, the phase angle is not 90 degrees at the natural frequency, in constrast to viscous damped systems. Second, the maximum phase angle is less than that reached by a viscous damped system having the same damping ratio.

The system response to a step function was determined from the square-wave input that had a duration sufficiently long to permit the transient decay. The square-wave was introduced into the control loop with a voltage amplitude corresponding to the desired step angular displacement of the test table. Adjustment of recorded data was made for any asymmetry of the sensor gain. For the same control loop settings as used in the previous frequency response data, the maximum overshoot was 36 percent and occurred at t = 0.72 second. This would indicate a damping ratio of 0.32. The natural frequency is

$$\omega_N = \frac{\pi}{\frac{t}{\sqrt{1 - c^2}}} = \frac{3.32}{0.72} = 4.62 \text{ rad/sec.}$$

A plot of the step response is shown in Figure 12. The rise time (10 to 90 percent) is 0.3 second, and the settling time to a ±7 percent tolerance zone is 1.8 seconds. The gain for these data is estimated at 465 ft-lb/rad. This corresponds to a sensor gain of 9.3 millivolts/arc-sec, indicating a step amplitude of 77 arc-seconds in Figure 12.

Table 1 summarizes the response to square-wave inputs at various test control loop gain settings. The first 11 columns represent observed test data. Damping ratio is determined from percentage of overshoot; settling times are presented in two ways. The first, percentage tolerance, allows direct comparison of settling times with other gains. The second, angular tolerance, indicates how well the various gains permitted settling to a given angular displacement, and is not for direct comparison. Ultimate settling indicates how well the system finally stabilized with each gain, without regard to a particular tolerance zone or settling time. Since the input square wave for all these data was at a constant frequency (0.04 Hz), the ultimate settling time available with each gain was 12.5 seconds. The determination of the values in the remaining columns of Table 1 is explained in Appendix A.

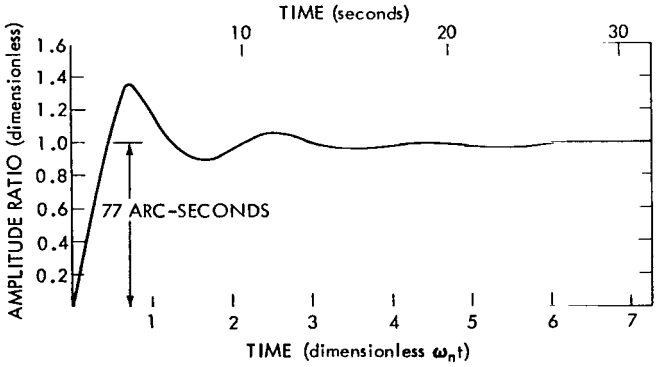

Figure 12 — System step response.

On the basis of data in the summary table, the best loop gain for this system was chosen to be 697 ft-lb/rad (computed loop gain).

It was desired to determine if the previously chosen test-loop parameters were adequate for spacecraft scanning missions. The most stringent control requirement in such missions is the relatively rapid turnaround of the spacecraft at the end of each constant angular velocity scan line. It was assumed that the turnaround must be performed in 4 seconds when the scan line velocity, ω_S, is 200 arc-sec/sec (9.69×10^{-4} rad/sec). Settling to a ±1 arc-second transient pointing error was considered adequate. Figure 13 shows the plot assumed to be the reference command for the turnaround axis. As seen in Figure 13, the required performance is settling from a step velocity change of 9.69×10^{-4} rad/sec in 1.33 seconds.

Universal curves for settling from a step velocity change were used to determine system response. Since damping ratio was previously determined to be 0.52, the universal curve for a damping ratio of 0.5 was used. The resulting peak position error, e, overshoot is

$$e(\max)\frac{\omega_N}{\omega_S} = 0.53$$

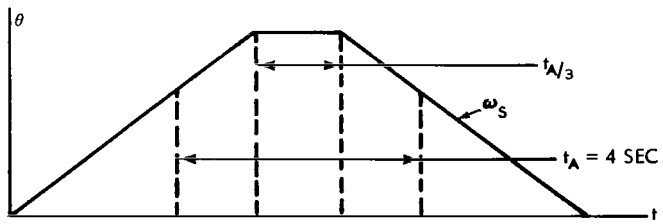

Figure 13 — Reversing diagram.

Table 1

Summary of Step Response at Various Gains

Autocollimator setting	Sensor gain (mv/arc-sec)	Step amplitude (arc-sec)	Maximum percentage overshoot (%)	Damping ratio	Rise time (sec)	Settling time ±7% (sec)	Settling time ±6.7 arc-sec (sec)	Ultimate settling			Observed loop gain, K (ft-lb/rad)	Computed loop gain, K' (ft-lb/rad)	Observed ω_N (rad/sec)	Computed ω_N (rad/sec)	Error rate gain (ft-lb/rad/sec)
								Amplitude (± arc-sec)	Frequency (Hz)	Remarks					
0.1	1.9	374	18	0.47	0.4	1.3	2.2	6.7	1.0	Oscillation sometimes increasing	345	232	3.7	3.0	71
0.2	3.7	192	10	0.60	0.3	0.9	2.1	4.7	1.0	Steady oscillation	747	465	5.5	4.3	130
0.3	5.6	128	15	0.52	0.2	0.7	0.8	2.8	1.0	Oscillation diminishing	942	697	6.1	5.3	137
0.4	7.4	96	19	0.46	0.4	1.1	1.1	2.4	1.0	Steady oscillation	1370	930	7.4	6.1	140
0.5	9.3	77	23	0.42	0.2	1.3	1.1	4.0	1.4	Steady oscillation	2250	1162	9.5	6.8	143
0.6	11.2	64	56	0.18	0.1	1.9	1.3	2.4	1.4	Steady oscillation	1450	1395	7.6	7.4	67
0.7	13.0	55	63	0.14	0.2		3.7	6.8	1.8	Oscillation sometimes increasing	1950	1628	8.8	8.1	56
0.8	14.9	48	100	0.01	0.1		7.1	6.8	2.1	Oscillation sometimes increasing	1400	1858	7.5	8.6	4

and

$$e(\max) = \frac{9.69 \times 10^{-4} \text{ rad/sec}}{5.3 \text{ rad/sec}} \quad (0.53)$$

$$= 0.976 \times 10^{-4} \text{ radians} = 20.1 \text{ arc-seconds.}$$

The resulting time for settling to 1 arc-second is $\omega_N t = 6.8$, or 1.3 seconds. Thus, the system meets the required turnaround performance. It should be noted that this performance is achievable without requiring optimization of the turnaround reference command.

CONCLUSION

The application of photoelectronic commutation techniques to a reaction wheel drive, complemented by optimized reaction wheel mechanical design, has yielded a basic reaction wheel design with superior characteristics. Significant savings in reaction wheel weight and power requirements were achieved. The photoelectronic commutator has allowed the consolidation of control system functions within the reaction wheel itself, thereby reducing overall system complexity and enhancing reliability. In addition, the photoelectronic commutator has provided state-of-the-art improvement in control system design by incorporating capabilities such as regenerative braking. The test program has shown that integration of the brushless reaction wheel into control systems capable of pointing precision within a few seconds of arc presents no unforeseen difficulties.

ACKNOWLEDGMENT

The author wishes to acknowledge the contribution of Mr. Philip A. Studer to this effort. Mr. Studer was instrumental in directing the design and development of the brushless dc torquer-driven reaction wheel.

Goddard Space Flight Center
National Aeronautics and Space Administration
Greenbelt, Maryland, September 23, 1968
125-19-05-08-51

APPENDIX A

Control System Testing

The first portion of this appendix concerns the test control system, and the remainder concerns the computation of step response data.

Control System Sensor and Electronics

The error characteristic of the test control system autocollimator sensor, with reference to the sensor null position, is shown in Figure A1. This characteristic is for the setting of the autocollimator amplifier indicated. The control electronics that process the sensor output are shown in Figure A2. These electronics were developed at Goddard Space Flight Center to facilitate adapting the reaction wheel to specific control applications. The electronics accept a plus or minus sensor input V_e and produce the three outputs to the wheel electronics shown in Figure A2. The torque magnitude output is a proportional dc signal, always positive polarity, that indicates the level of torque required. The torque direction command outputs are complementary logic signals that indicate the required sense of the torque. The rotational-losses-compensation output is a low-level dc signal that greatly reduces the small step in output torque which torquers typically exhibit when passing through zero speed (0.023 foot-pound for the brushless dc torquer). Figure A3 shows the control loop compensation provided in the error signal processor of the control electronics. The transfer function of this equivalent circuit is

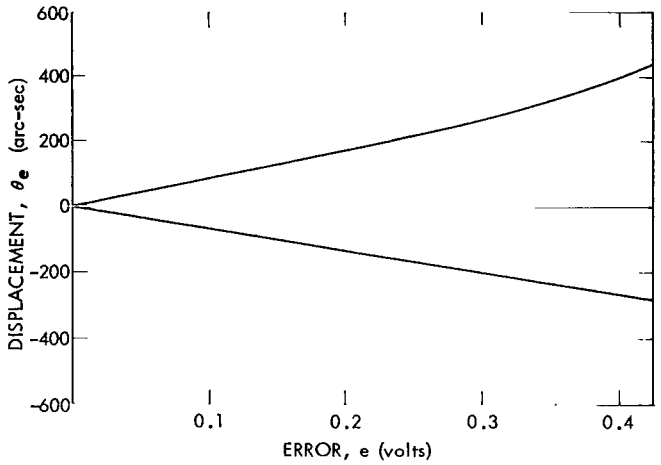

Figure A1 — Autocollimator error characteristic (autocollimator setting of 0.0625).

$$G(S) = \left(\frac{1}{3.5}\right)\left(\frac{1 + 0.613S}{1 + 0.175S}\right).$$

Computation of Step Response Data

The values concerning step response performance are determined as follows.

Observed ω_N

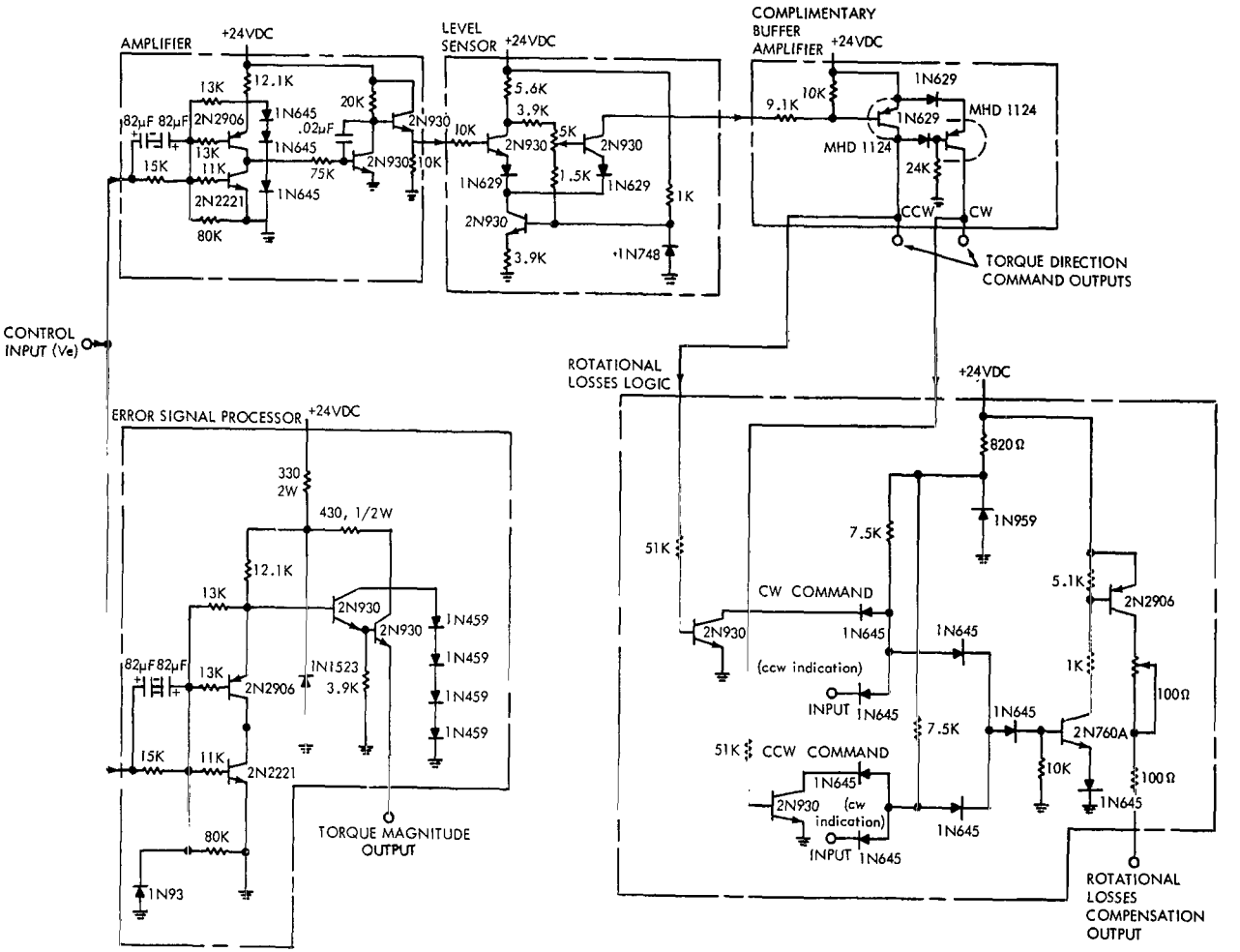

Figure A2 — Control electronics schematic diagram.

This contrasts with the below Computed ω_N in that measured values associated with each loop gain were used in the computation. These values are the damping ratio c, determined from peak overshoot, and the time of peak overshoot t. They were used in

$$\omega_N = \frac{\frac{1}{1-c^2}}{t}.$$

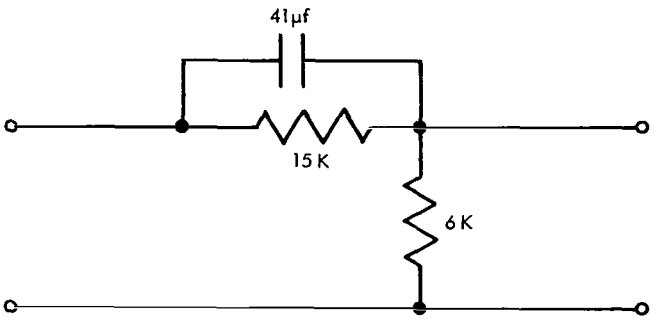

Figure A3— Error rate network.

Observed loop gain, K

Since J was known to be 25 slug-ft^2, K was computed using the preceding Observed ω_N in $K = \omega_N{}^2 J$.

Computed loop gain, K'

This gain was computed from the product of sensor gain, operational amplifier gain, and control and wheel electronics gain. From the control loop gain characteristic, the last term was determined to be 0.12 ft-lb/volt. The operational amplifier gain was kept at 5 for all loop gains.

Computed ω_N

This was computed using $\omega_N = \sqrt{K/J}$. The preceding Computed loop gain was used for K.

Error rate gain, L

Since viscous damping was assumed to be negligible, L was computed using $L = 2Jc\omega_N$. The damping ratio, obtained as previously mentioned, and Computed ω_N were used.

"The aeronautical and space activities of the United States shall be conducted so as to contribute . . . to the expansion of human knowledge of phenomena in the atmosphere and space. The Administration shall provide for the widest practicable and appropriate dissemination of information concerning its activities and the results thereof."

—NATIONAL AERONAUTICS AND SPACE ACT OF 1958

NASA SCIENTIFIC AND TECHNICAL PUBLICATIONS

TECHNICAL REPORTS: Scientific and technical information considered important, complete, and a lasting contribution to existing knowledge.

TECHNICAL NOTES: Information less broad in scope but nevertheless of importance as a contribution to existing knowledge.

TECHNICAL MEMORANDUMS: Information receiving limited distribution because of preliminary data, security classification, or other reasons.

CONTRACTOR REPORTS: Scientific and technical information generated under a NASA contract or grant and considered an important contribution to existing knowledge.

TECHNICAL TRANSLATIONS: Information published in a foreign language considered to merit NASA distribution in English.

SPECIAL PUBLICATIONS: Information derived from or of value to NASA activities. Publications include conference proceedings, monographs, data compilations, handbooks, sourcebooks, and special bibliographies.

TECHNOLOGY UTILIZATION PUBLICATIONS: Information on technology used by NASA that may be of particular interest in commercial and other non-aerospace applications. Publications include Tech Briefs, Technology Utilization Reports and Notes, and Technology Surveys.

Details on the availability of these publications may be obtained from:

SCIENTIFIC AND TECHNICAL INFORMATION DIVISION

NATIONAL AERONAUTICS AND SPACE ADMINISTRATION

Washington, D.C. 20546